SILLi 1.0: A 1D Numerical Tool Quantifying the Thermal Effects of Sill Intrusions

*Karthik Iyer[1,2], Henrik Svensen[3] and Daniel W. Schmid[1,4]

*karthik.iyer@geomodsol.com

1 GeoModelling Solutions GmbH, Zurich, Switzerland

2 GEOMAR, Helmholtz Centre for Ocean Research, Kiel, Germany

3 Centre for Earth Evolution and Dynamics, University of Oslo, Norway

4 Physics of Geological Processes, University of Oslo, Norway

Abstract

Igneous intrusions in sedimentary basins may have a profound effect on the thermal structure and physical properties of the hosting sedimentary rocks. These include mechanical effects such as deformation and uplift of sedimentary layers, generation of overpressure, mineral reactions and porosity evolution, and fracturing and vent formation following devolatilization reactions and the generation of CO_2 and CH_4. The gas generation and subsequent migration and venting may have contributed to several of the past climatic changes such as the end-Permian event and the Paleocene-Eocene Thermal Maximum. Additionally, the generation and expulsion of hydrocarbons and cracking of pre-existing oil reservoirs around a hot magmatic intrusion is of significant interest to the energy industry. In this paper, we present a user-friendly 1D FEM based tool, SILLi, which calculates the thermal effects of sill intrusions on the enclosing sedimentary stratigraphy. The model is accompanied by three case studies of sills emplaced in two different sedimentary basins, the Karoo Basin in South Africa and the Vøring Basin offshore Norway. Input data for the model is the present-day well log or sedimentary column with an Excel input file and includes rock parameters such as thermal conductivity, total organic carbon (TOC) content, porosity, and latent heats. The model accounts for sedimentation and burial based on a rate calculated by the sedimentary layer thickness and age. Erosion of the sedimentary column is also included to account for realistic basin evolution. Multiple sills can be emplaced within the system with varying ages. The emplacement of a sill occurs instantaneously. The model can be applied

28 to volcanic sedimentary basins occurring globally. The model output includes the thermal evolution of

29 the sedimentary column through time, and the changes that take place following sill emplacement such

30 as TOC changes, thermal maturity, and the amount of organic and carbonate-derived CO_2. The TOC and

31 vitrinite results can be readily benchmarked within the tool to present-day values measured within the

32 sedimentary column. This allows the user to determine the conditions required to obtain results that

33 match observables and leads to a better understanding of metamorphic processes in sedimentary

34 basins.

35

1   Introduction

37 Volcanic processes can strongly influence the development of sedimentary basins associated with

38 continental margins. Magmatic bodies such as dikes and sills have a major impact on the thermal

39 evolution of these sedimentary basins. The short-term effects of igneous intrusions include deformation

40 and uplift of the intruded sediments, heating of the host rock, mineral reactions, generation of

41 petroleum, boiling of pore fluids and possible hydrothermal venting (Jamtveit et al., 2004; Malthe-

42 Sorenssen et al., 2004; Svensen et al., 2004; Wang et al., 2012b). Long-term effects include focused fluid

43 flow, migration of hydrothermal and petroleum products, formation of mechanically strong dolerite and

44 hornfels in the contact aureole and differential compaction (Iyer et al., 2013; Iyer et al., 2017; Kjoberg et

45 al., 2017; Planke et al., 2005). This is of particular importance to understanding the carbon cycle, as

46 thermal stresses, besides those associated with burial, encountered by organic matter in immature

47 source rocks will determine the ultimate production and fate of the CO_2 and CH_4 generated. Vent

48 structures are intimately associated with sill intrusions in sedimentary basins globally and are thought to

49 have been formed contemporaneously due to overpressure generated by pore-fluid boiling gas

50 generation during thermogenic breakdown of kerogen (Aarnes et al., 2015; Iyer et al., 2017; Jamtveit et

51 al., 2004). Methane and other gases generated during this process may have driven catastrophic climate

52 change in the geological past (Svensen and Jamtveit, 2010; Svensen et al., 2009). Magmatic intrusions

53 are also of particular interest for hydrocarbon prospectivity and can impact petroleum systems in

54 positive and negative ways (Archer et al., 2005; Monreal et al., 2009; Peace et al., 2017). High

55 temperatures in the thermal aureole around such intrusions may induce maturation and hydrocarbon

56 generation in immature, shallow strata that may have not been productive under normal burial. On the

57 other hand, pre-emptive maturation of hydrocarbons around an intrusion may result in loss of

58 hydrocarbons if a suitable reservoir has not yet formed. Additionally, pre-existing oil in a reservoir may

59 crack to gas in the vicinity of magmatic intrusions resulting in degradation of a potential prospect. In

60 order to understand these problems, numerical models are widely used to reconstruct the thermal

61 history of a basin where only a few of these parameters are known.

62 A number of analytical and numerical models have been developed that study the thermal effects of

63 igneous intrusions dating back to the early- and mid-1900's (Jaeger, 1964; Jaeger, 1957, 1959; Lovering,

64 1935). Subsequent 1D and 2D models added additional complexity to the models by the addition of

65 emplacement mechanisms and timing, source rock maturation, hydrocarbon generation, latent heats of

66 devolatilization and maturation, fluid processes and overpressure generation (Aarnes et al., 2011a;

67 Fjeldskaar et al., 2008; Galushkin, 1997; Iyer et al., 2017; Monreal et al., 2009; Wang, 2013; Wang, 2012;

68 Wang et al., 2010; Wang and Song, 2012; Wang et al., 2012a). Contact metamorphic processes are well

69 understood (e.g. (Aarnes et al., 2010; Jamtveit et al., 1992; Tracy and Frost, 1991)), but many published

70 papers do not take into account the basin history or the variations in contact aureole thickness that arise

71 from the type of measuring method that has been used. In general, the contact metamorphic effects

72 depend on 1) sill thickness (note that dikes cannot be directly compared with sills), 2) sill emplacement

73 temperature, 3) thermal gradient and emplacement depth (i.e. temperature and background

74 maturation), 4) emplacement history (instantaneous versus prolonged magma flow), 5) host rock

75 composition and characteristics (such as thermal conductivity, organic carbon content, porosity,

76 permeability) and 6) conductive versus advective cooling (e.g. (Aarnes et al., 2010; Galushkin, 1997; Iyer

77 et al., 2013; Iyer et al., 2017; Jaeger, 1964; Lovering, 1935; Wang, 2012)). In addition, the contact

78 aureole width depends on how aureoles are studied and measured. The aureole thickness depends on

79 the proxy used, including sonic velocity, density, mineralogy and mineral properties, magnetic

80 susceptibility, total organic carbon content, vitrinite reflectivity, color, porosity, or organic geochemistry.

81 Note that these aureole thickness proxies will not necessarily give the same result. Finally, the aureole

82 thickness also depends on the proximity to other sills emplaced at the same time (see Aarnes et al.

83 (2011b) for a quantification).

84 In this paper we present a generic 1D thermal model, SILLi, which can be applied to studying the thermal

85 effects of sill intrusions in sedimentary basins globally. The motivation behind the model and manuscript

86 is to make a standardized numerical toolkit openly available that can be widely used by scientists with

87 varying backgrounds to test the effect of magmatic bodies in a wide variety of settings using readily

88 available data such as standard well logs and field measurements. The model incorporates relevant

89 processes associated with heat transfer from magmatic intrusions such as latent heat effects,

90 decarbonation reactions and organic matter maturation and also accounts for background maturation

91 and erosion by systematically reconstructing the entire present-day sedimentary column from the input

92 data. Lastly, the model results can be easily compared to the two most widely used aureole proxies in

93 sedimentary rocks, vitrinite reflectance (VR) and total organic carbon (TOC) data.

94

2   Model Input

96 The one dimensional, Finite Element Method (FEM) model numerically recreates the thermal effects of

97 sill emplacement in a sedimentary column. The model is written using MATLAB and requires version

98 2014b or higher to run. The model input is specified in an Excel (*.xls) file and is read by the Matlab file,

99 SILLi.m. The user also specifies the model resolution with the igneous intrusions and sedimentary layers

100 by giving the minimum spacing (m) or the minimum number of points in the Matlab file. The measure

101 that produces the highest resolution is used. The Excel file is composed of seven tabs outlined below. If

102 a previously calculated output file is available for the input file, the program prompts the user to choose

103 between loading the output file for further analysis and performing a new calculation which overwrites

104 the existing file.

105 For correct model use, the geological input needs to be based on either a borehole (with horizontal

106 stratigraphy) or an outcrop that is converted into a pseudo-borehole. If the case study is outcrop-based,

107 a pseudo-borehole stratigraphy should be constructed including the regional basin stratigraphy. Note

108 that sedimentary rocks present at higher stratigraphic levels elsewhere in the basin should be added to

109 the erosion history of the basin. Moreover, the sills (and samples) should be rotated back to horizontal if

110 the stratigraphy was tilted post sill emplacement. Using TOC and VR data from sedimentary rocks

111 outside the immediate contact aureoles will improve the model calibration.

112

2.1   Fluid

114 This tab contains four columns describing the fluid name, its density (kg/m^3), heat capacity (J/kg/K) and

115 thermal conductivity (W/m/K).

116

2.2 Lithology

This tab contains the data required for the model to build the present-day sedimentary column. The various columns detail the name of the sedimentary layer (character only) and various material properties such as density (kg/m^3), heat capacity (J/kg/K), porosity (fraction), thermal conductivity (W/m/K), initial TOC content (wt%) and latent heats of organic maturation and dehydration (kJ/kg). Information regarding the kind of carbonate contained in the sedimentary layer can be given in the last column if decarbonation reactions are considered. The mineral constitution of the carbonate can be chosen as marl (1), dolomite (2) or dolomite/evaporite mix (3). A zero (0) is entered in this column if decarbonation reactions are not required. The lithology tab also contains columns where the present-day top depth (m) and age (Ma) of each layer can be given which determine the depositional sequence and sedimentation rate for the layer (see Section 3.1). Note that the ages of the sedimentary must be unique. A hypothetical basement is added 10 m below the deepest sedimentary layer top depth.

2.3 Erosion

This tab is similar to the lithology tab and contains information on eroded layers. Additional columns in this tab contain information regarding the erosion timing (Ma) and the thickness of the eroded layer (m). Note that the top depth of the eroded layer must coincide with the top of a sedimentary layer in the lithology tab. If part of sedimentary layer is indeed eroded before deposition continues (i.e. the eroded layer lay inside a deposited layer), the layer needs to be considered as unique layers separated by the eroded layer. Multiple eroded layers can have the same top depths provided that older layers with the same top depth are eroded first. Similarly, eroded layers have to be eroded first prior to deposition of younger layers. The ages of the eroded layers cannot coincide with other layers.

2.4 Sills

This tab contains information necessary for the emplacement of sill intrusions. The top depth (m) and thickness (m) of the sill constrain the geometry of the intrusion. Additional information includes the time of emplacement (Ma), emplacement temperature (°C), melt and solid densities (kg/m^3), melt and solid heat capacities (J/kg/K), thermal conductivity (W/m/K), solidus and liquidus temperatures of the magma (°C) and the latent heat of crystallization (kJ/kg). The emplacement of the intrusion is assumed to be instantaneous. Note that the top depth of the sill cannot be the same as the top depth of a

147 sedimentary layer. On the same note, the top depth of a sedimentary layer cannot be inside a sill

148 intrusion. Emplacement ages cannot exactly coincide with layer ages.

149

2.5   Temperature Data

151 This tab contains temperature data (°C) vs. depth (m) for the sedimentary column. The data in this tab is

152 used to construct a geothermal gradient by using the best linear fit and therefore needs to contain at

153 least two data points. Additionally, the first data point must coincide with the column top describing the

154 surface temperature.

155

2.6   Vitrinite Data (Optional)

157 This tab contains present day vitrinite reflectance data presented in depth (m) and VR values (%Ro).

158 Standard deviation of the values when available can be included. This data is used for comparison of the

159 modelled VR values to observations. This tab can be left blank if no measured information is available.

160

2.7   TOC Data (Optional)

162 This tab contains present day TOC content data (wt%) vs. depth (m) measured in the sedimentary

163 column which is used to compare to the model results. This tab can be left blank if no measured

164 information is available.

165

3   Method

3.1   Sediment Deposition and Erosion

168 Each sedimentary layer, including the eroded layers, is deposited sequentially in time based on the

169 depositional age. The rate of sedimentation for each layer is determined by the thickness of the layer

170 and the difference in time between its top age and that of the layer deposited before it. Erosional layers

171 in the sedimentary column are deposited in the same way as other layers. Erosion of the entire layer

172 occurs within a single step at the specified erosion age. The temperature boundary conditions are

173 accordingly adjusted for the height of the new sedimentary column. Note that the bottom boundary is

174   extended to 5 times the thickness of the bottommost sill if that sill is close to or at the bottom boundary

175   (hypothetical basement) in order to remove boundary effects and resolve aureole processes that are

176   mostly limited to less than 4 times the sill thickness (Aarnes et al., 2010).

177

3.2   Thermal Diffusion

179   The thermal solver computes the temperature within the deposited sedimentary column by applying

180   fixed temperatures at the top and bottom at every step which are calculated from the prescribed

181   geotherm (see Section 2.5) and the energy diffusion equation,

182
$$\left[\phi \rho_f c_{pf} + \left(1-\phi\right) \rho_r c_{peff} \right] \frac{\partial T}{\partial t} = \nabla \cdot \left(\kappa_{eff} \nabla T \right) \tag{1}$$

183   κ_{eff} is the bulk thermal conductivity that includes the rock and fluid contributions as a geometric mean

184   (Hantschel and Kauerauf, 2009):

185
$$\kappa_{eff} = \kappa_r^{(1-\phi)} \kappa_f^{\phi} \tag{2}$$

186   Table 1 contains the definitions of all the notations used in the manuscript. The effective rock heat

187   capacity accounts for the latent heat of fusion in the crystallizing parts of the sill between the solidus (T_S)

188   and liquidus (T_L) temperature of the magma (e.g. (Galushkin, 1997))

189
$$c_{peff} = c_{pm} \left[1 + \frac{L_c}{\left(T_L - T_S\right) c_{pm}} \right] \text{ if } \left[T_S < T < T_L \right]$$
$$c_{peff} = c_{pr} \qquad\qquad \text{ if } \left[T_S > T \right] \tag{3}$$

190   Sills are emplaced instantaneously at the specified time and temperature within the sedimentary

191   column. The emplacement of multiple sills in the same step is possible. The time-steps used for thermal

192   diffusion after sill emplacement are automatically calculated based on the sill thickness and the

193   characteristic time required for thermal diffusion. The time step is initially small in order to accurately

194   resolve the thermal evolution of the contact aureole around the sill and is gradually increased once the

195   energy released by the cooling sill is dissipated.

196   Dehydration reactions in the host rock are implemented by modifying the thermal diffusion equation

197   when temperatures of the sediments increase within a certain range (Galushkin, 1997; Wang, 2012)

$$198 \qquad \left[\phi \rho_f c_{pf} + (1-\phi)\rho_r c_{peff}\right]\frac{\partial T}{\partial t} = \nabla \cdot (\kappa \nabla T) - H \qquad (4)$$

$$199 \qquad H = \frac{(1-\varphi)\rho_r L_d}{T_{d1} - T_{d2}}\frac{\partial T}{\partial t} \qquad (5)$$

Symbol	Description	Units
A	Frequency factor	s^{-1}
c_{peff}	Effective rock heat capacity	$J\,kg^{-1}\,K^{-1}$
c_{pf}	Fluid heat capacity	$J\,kg^{-1}\,K^{-1}$
c_{pr}	Rock heat capacity	$J\,kg^{-1}\,K^{-1}$
E	Activation energy	$KJ\,mol^{-1}$
f	Stoichiometric factor	
F	Reaction extent	
g	Gravitational acceleration	$m\,s^{-2}$
i	Reactive component	
L_c	Latent heat of crystallization	$KJ\,kg^{-1}$
m_{CO_2}	Carbon to CO_2 conversion factor	3.66
P_{atm}	Atmospheric pressure	10^5 Pa
P_{H2O}	Hydrostatic pressure	Pa
R_{CO_2}	Rate of CO_2 generation	$kg\,m^{-3}\,s^{-1}$
R_{om}	Rate of organic matter degradation	$kg\,m^{-3}\,s^{-1}$
t	Time	s
T_L	Liquidus temperature	°C
T_S	Solidus temperature	°C
T	Temperature	°C
$T_{d2} - T_{d1}$	Temperature range for dehydration reactions (Galushkin, 1997)	350-650 °C
w	Amount of reactive component	Fraction
Z	Depth	km
ϕ	Rock porosity	Fraction
κ_{eff}	Bulk thermal conductivity	$W\,m^{-1}\,K^{-1}$

κ_r	Rock thermal conductivity	W m^{-1} K^{-1}
κ_f	Fluid thermal conductivity	W m^{-1} K^{-1}
ρ_f	Fluid density	kg m^{-3}
ρ_r	Rock density	kg m^{-3}

200   *Table 1. Definition of symbols used in the model.*

201

3.3   Thermal Maturation of Organic Matter

203   Vitrinite reflectance is a widely used indicator of thermal maturity and can be readily measured in the
204   field. One of the most common methods used to calculate the thermal maturity of the source rock is the
205   EASY%Ro method put forward by Sweeney and Burnham (1990). This model uses 20 parallel Arrhenius-
206   type of first order reactions to describe the complex process of kerogen breakdown due to temperature
207   increase. The reaction for the ith component is given by

208
$$\frac{dw_i}{dt} = -w_i A \exp\left[-\frac{E_i}{RT^t}\right] \tag{6}$$

209   where w_i is the amount of material for component i, E_i is the activation energy for the given reaction and
210   T^t is time-dependent temperature.

211   The total amount of material reacted is obtained by summing up the individual reactions

212
$$\frac{dw}{dt} = \sum_i \frac{dw_i}{dt} \tag{7}$$

213   The fraction of reactant converted is

214
$$F = 1 - \frac{w}{w_0} = 1 - \sum_i f_i \left(\frac{w_i}{w_{0i}}\right) \tag{8}$$

215   from which the vitrinite reflectance can be readily calculated by

216
$$\% Ro = \exp\left(-1.6 + 3.7F\right) \tag{9}$$

217   The amount of TOC that has reacted for any given time can be calculated by

218
$$\text{TOC}(t) = \text{TOC}_o F(t) \tag{10}$$

219   and the rate of organic matter degradation by

220
$$R_{om} = (1-\phi)\rho_r \frac{\partial \text{TOC}}{\partial t} \tag{11}$$

221   The maximum amount of TOC that can be reacted by this method is 85% of the initial total. Note that in
222   the inner part of the contact aureole close the sill, data shows that all of the organic matter has been
223   reacted or removed (eg. LA1/68 in section 5.2.2). We assume that all of the hydrocarbons released
224   during thermal degradation are converted into carbon dioxide. The amount of organic carbon dioxide
225   generated (R_{CO2}) for a time step is given by

226
$$R_{CO_2} = R_{om} m_{CO_2} \tag{12}$$

227   where m_{CO2} is a stoichiometric conversion factor (3.67) to transform carbon into carbon dioxide. Note
228   that metamorphism of sedimentary rocks will generate CH_4 (e.g., (Aarnes et al., 2010; Iyer et al., 2017)),
229   but in our model the reacted carbon is recalculated to CO_2. If needed, the CO_2 model output can be
230   easily converted to either C or CH_4.

231   The latent heat of organic maturation is accounted for in the energy equation

232
$$\left[\phi \rho_f c_{pf} + (1-\phi) \rho_r c_{peff} \right] \frac{\partial T}{\partial t} = \nabla \cdot (\kappa \nabla T) - H - L_{om} R_{om} \tag{13}$$

233

3.4 Mineral Decarbonation

235   Carbonate minerals undergo decarbonation reactions as they are heated to high temperatures. This
236   results in mineral transformations and the release of inorganic carbon dioxide which may significantly
237   add to the CO_2 budget associated with igneous intrusions. The amount of inorganic CO_2 liberated during
238   metamorphic transformation over a range of temperature and fluid pressure for marl, dolomite and
239   dolomite/evaporite mixture is pre-computed as a phase diagram using Perple_X (Connolly and Petrini,
240   2002) (Figure 1). The model evaluates the total amount of inorganic CO_2 liberated by carbonate layers
241   based on the temperature and pressure evolution of the layer through time within the phase diagrams.

242   Fluid pressure within the sedimentary column is calculated by integrating the rock density over depth in

243   addition to atmospheric pressure:

244
$$P_{H_2O} = P_{atm} + \int_{Z_{min}}^{Z_{max}} \rho_f \, \vec{g}$$
(14)
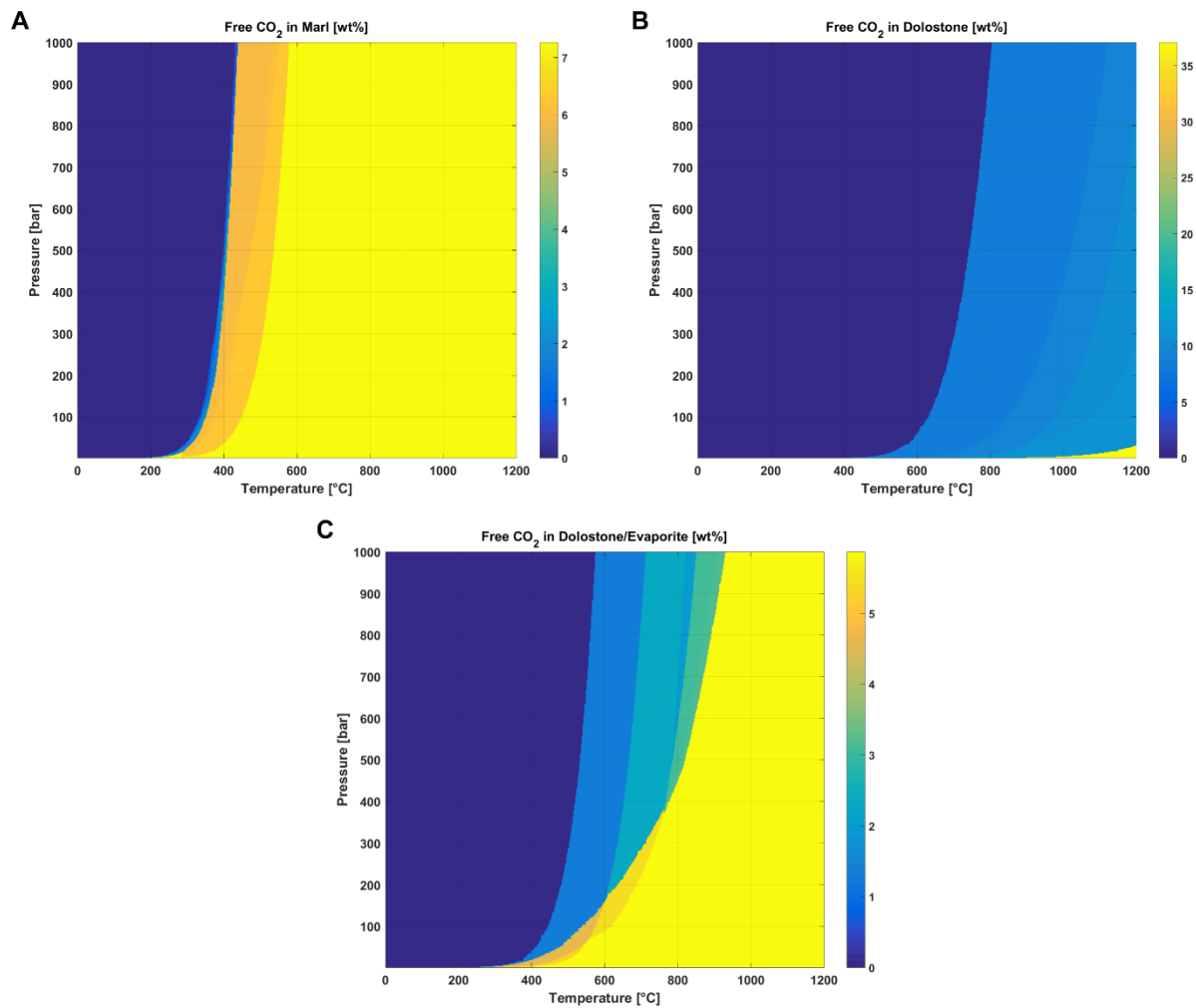
245

246   *Figure 1. Phase diagrams generated by Perple_X showing the amounts of inorganic CO_2 liberated with*

247   *respect to temperature and pressure for marl (A), dolostone (B) and dolostone/evaporite (C).*

248

3.5   Model Mesh and Time-Stepping

250   The entire sedimentary column including the eroded layers and igneous intrusions is reconstructed and

251   the column nodes and elements for the FEM model are generated using the user-specified resolution.

252 The nodes are initially collapsed onto each other in depth. Each sedimentary node is assigned a time

253 during which it is expanded (or deposited) within the sedimentary column based on the layer age and its

254 thickness. All of the elements and nodes associated with each igneous intrusion are expanded

255 simultaneously during the corresponding emplacement time. Eroded layers are removed in a single time

256 step specified by the erosion age and the corresponding nodes are collapsed. In order to correctly

257 capture thermal diffusion across the large thermal gradient adjacent to a hot intrusion, the time step is

258 initially very small and exponentially increases during the heating period after sill emplacement and

259 before the next depositional event. The heating period of the sill, over which the exponential time sub-

260 stepping is used, is analytically determined from the characteristic diffusion time for the sill thickness

261 (Jaeger, 1959).

262

3.6 Model Limitations

263

264 • The model is one-dimensional and will therefore not resolve thermal effects that would require

265   a full 3D model.

266 • The model does not account for advective transport of heat through the system by fluids.

267   However, previous models have shown that this process would be dominant only in high

268   permeability systems or at the sill edges/tips in low permeability systems (Iyer et al., 2013; Iyer

269   et al., 2017). Therefore, the model presented in this manuscript works well for relatively low

270   permeability systems with shales, mudstone etc. and when the sedimentary column passes

271   through the sill interior away from the edges. Nevertheless, in some cases the effects of

272   hydrothermal activity may be visible where the thermal aureole is larger above than below the

273   sill and is recorded by vitrinite reflectance data (Galushkin, 1997; Wang and Manga, 2015). In

274   such cases, the user may use an enhanced thermal conductivity (up to 5 times the usual rock

275   conductivity) in the layer above the sill following the Nusselt number approach to account for

276   hydrothermal activity and match field data. Note that care should be taken to check if the same

277   effect can also be attributed to changes in other material properties or geological processes.

278 • The model does not account for other mineral reactions in the contact aureole besides

279   decarbonation of carbonates. The various mineral reactions possible in the contact aureole can

280   be implemented as an add-on module to the model if needed using the thermal evolution of the

281   sedimentary column obtained from the model. Similarly, correlation to other maturity

282   parameters such as mineralogical markers or biomarkers (e.g. Muirhead et al. (2017)) can be
283   performed by the user using the time-temperature evolution from the model if so desired.

284   •   The model assumes that TOC conversion in all types of sedimentary rocks can be estimated by
285   using the EASY%Ro method with a maximum conversion value of 85%. Although, this is a good
286   first approximation, it cannot account for the complete loss of carbon in zones very close to the
287   sill-host rock interface which would result in an underestimation of the released gases (Svensen
288   et al., 2015). On the other hand, the provenance of the sedimentary rock can also significantly
289   affect how kerogen present in organic matter reacts to form hydrocarbons which may result in a
290   reduction in the amount of convertible organic matter due to the presence of inert kerogen (Iyer
291   et al., 2017; Pepper and Corvi, 1995).

292

4   Model Output

294 The model input and results are presented with the help of a GUI (Section 4.6). Model data are written
295 out as a single .mat (Matlab data) file in the same directory as the user-defined path for the input Excel
296 file and with the same filename. The file contains five 'struct' variables of which three contain input
297 information (rock, sill and welldata) and the other two contain model results (result and release). The
298 structure of the variables are described below.

299

4.1   Struct Variable: rock

301 This variable contains input information on the sedimentary layers in the column including the eroded
302 layers. The information is saved as variables given in Table 2 and is sorted according to their top depths.
303 Note that top depths are corrected for the eroded layers that are also included.

Variable Name	Description
Name	User-defined names of all the sedimentary layers in the column.
num	Total number of deposited sedimentary layers.
top	Top depth of the shallowest sedimentary layer.
bot	Top depth of the deepest sedimentary layer.
Tops	Top depths of sedimentary layers.
Ages	Ages of sedimentary layers.

Variable Name	Description
Rho	Density of sedimentary layers.
Cp	Heat capacity of sedimentary layers.
Phi	Porosity of sedimentary layers.
K	Thermal conductivity of sedimentary layers.
Toc	TOC content of sedimentary layers.
Lm	Latent heat of maturation of sedimentary layers.
Ld	Latent heat of dehydration of sedimentary layers.
Carb	Carbonate layer identifier (0-3).
Ero_t	Erosion age of sedimentary layers (NaN if layer is not eroded).
Ero_thick	Eroded thickness of sedimentary layers (NaN if layer is not eroded).
Ero_tops	Top depths of the eroded layers only.

304 *Table 2. List of variables in 'rock' struct variable of the output file.*

305

4.2   Struct Variable: sill

307 This variable contains input information on sill intrusions in the column. The information is saved as
308 variables given in Table 3 and is sorted according to their top depths.

Variable Name	Description
num	Total number of sill intrusions.
Tops	Top depths of sill intrusions.
E_time	Emplacement ages of sill intrusions.
E_temp	Emplacement temperatures of sill intrusions.
Rhom	Melt density of sill intrusions.
Cpm	Melt heat capacity of sill intrusions.
Rhos	Solid density of sill intrusions.
Cps	Solid heat capacity of sill intrusions.
K	Thermal conductivity of sedimentary layers.
Sol	Solidus of melt in sill intrusions.
Liq	Liquidus of melt in sill intrusions.
Ld	Latent heat of crystallization of melt in sill intrusions.

309 *Table 3. List of variables in 'sill' struct variable of the output file.*

310

4.3   Struct Variable: welldata

312 This variable contains input information on measured TOC, VR and temperature data for the
313 sedimentary column. The information is saved as variables given in Table 4.

Variable Name	Description
TOC	Measured TOC data vs. depth.
VR	Measured VR data vs. depth.
T	Measured temperature data vs. depth.

314 *Table 4. List of variables in 'welldata' struct variable of the output file.*

315

4.4   Struct Variable: result

317 This variable contains the model results which are saved for every time step when applicable, i.e.
318 variables that change over time have rows corresponding to the element or node number (depending
319 on where they are defined) and columns corresponding to the time step number. The information is
320 saved as variables given in Table 5.

Variable Name	Description (Rows x Columns)
nel	Number of elements in the model (1 x 1)
nnod	Number of nodes in the model (1 x 1)
Gcoord_c	Depth of element centers (1 x no. of elements)
Ind	Internal nodal indexing of sedimentary layers and intrusions (no. of nodes x 1). Intrusions are negatively indexed.
Ind_nel	Internal element indexing of sedimentary layers and intrusions (no. of elements x 1). Intrusions are negatively indexed.
Ind_carb	Nodal indexing of carbonate layers (0-3) (no. of nodes x 1).
Gcoord	Depth of nodes (no. of nodes x no. of time steps).
Temp	Nodal temperature (no. of nodes x no. of time steps).
Pres	Nodal hydrostatic pressure (no. of nodes x no. of time steps).

Toc	Remaining Toc content at nodes (no. of nodes x no. of time steps).
CO2_org	Organic carbon dioxide generated at nodes (no. of nodes x no. of time steps).
Ro	VR at nodes (no. of nodes x no. of time steps).
Tmax	Maximum temperature experienced at nodes (no. of nodes x no. of time steps).
Active	Binary index of 'deposited/expanded' nodes (no. of nodes x no. of time steps).
CO2_release	Inorganic carbon dioxide generated at nodes (no. of nodes x no. of time steps).
Time	Year count for time step (no. of time steps x 1).

Table 5. List of variables in 'result' struct variable of the output file.

4.5 Struct Variable: release

This variable contains the amounts of CO_2 released for every time step normalized to rock volume. The information is saved as variables given in Table 6.

Variable Name	Description (Rows x Columns)
CO2_org	Organic carbon dioxide generated in elements normalized to rock volume (no. of elements x no. of time steps).
CO2_rel	Inorganic carbon dioxide generated in elements normalized to rock volume (no. of elements x no. of time steps).

Table 6. List of variables in 'release' struct variable of the output file.

4.6 Output Graphical User Interface (GUI)

The GUI presented during and after the model run contains three tabs containing graphical representations of the input data, time evolution of model results and CO_2 release through time. An explanation of the tabs is given below using a hypothetical test case consisting of a sedimentary column with two sill intrusions and three eroded layers.

4.6.1 Input Tab

The left-most subplot of the input tab contains the reconstructed sedimentary column where the layers are colored according to their depositional age (http://www.stratigraphy.org/index.php/ics-chart-timescale) (Figure 2). The sedimentary column also contains eroded layers (hatched) and sill intrusions (speckled). The name and depositional age of a layer can be found by right-clicking the layer. The other

338   subplots in the input tab contain information on the density, porosity, initial TOC content and thermal
339   conductivity of the sedimentary layers. The values of these variables are plotted at the corresponding
340   layer top depth.
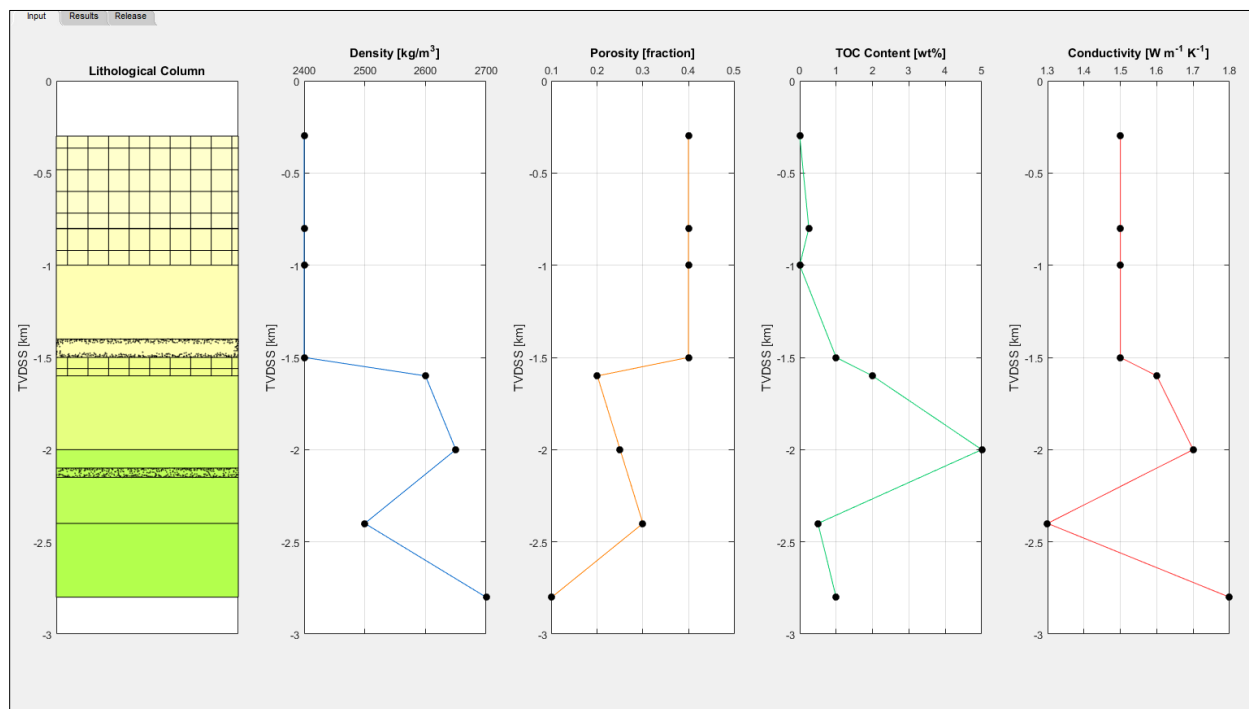
341

342   *Figure 2. Snapshot of the input tab generated for a hypothetical sedimentary column with two sill*
343   *intrusions and three eroded layers. Right-clicking a layer in the sedimentary column provides the name*
344   *and depositional/erosional age of the layer.*

4.6.2   Results Tab

346   The results tab consists of the evolution of temperature, vitrinite reflectance, TOC content, maximum
347   temperature, hydrostatic pressure, inorganic and organic CO_2 release within the sedimentary column
348   over simulated time (Figure 3). The evolution of these variables can be played or stepped through using
349   the player controls in the top left corner. Alternatively, the user can jump directly to the desired
350   geological time by inputting it in the player control. Note that this results in the plot jumping to the
351   time-step nearest the desired time input. Regions containing sill intrusions are highlighted in gray. Users
352   can copy plot data at any time step by right-clicking the curve.

353
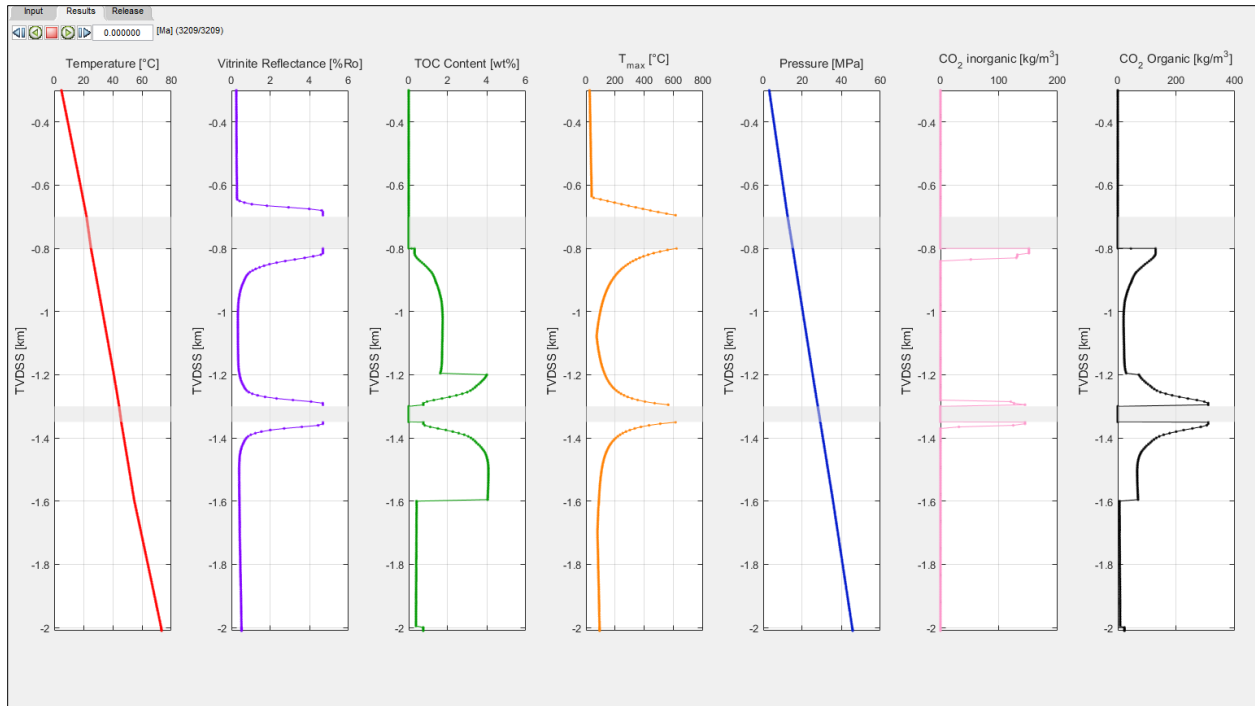
Figure 3. Snapshot of the results tab generated for a hypothetical sedimentary column with two sill intrusions and three eroded layers. Right-clicking any curve allows the user to copy curve data.

4.6.3   Release Tab

The release tab plots the cumulative and rates of release of organic and inorganic CO_2 due to heating of the sedimentary layer by sill intrusions (Figure 4). The cumulative and release rates are summed over the entire sedimentary column. The user can use the cumulative amount of gas released to easily upscale to basin scales by multiplying the value by the area affected by sill intrusions. Users can copy plot data at any time step by right-clicking the curve.

362
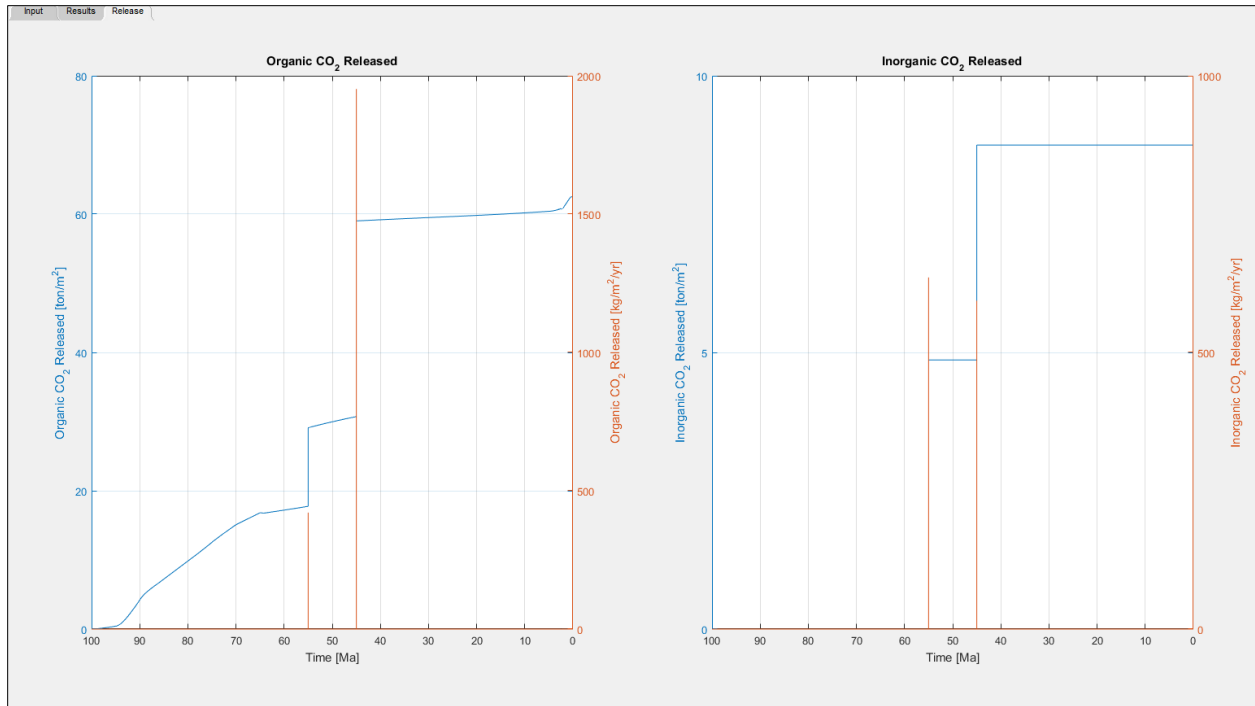
Figure 4. Snapshot of the release tab generated for a hypothetical sedimentary column with two sill
intrusions and three eroded layers. Right-clicking any curve allows the user to copy curve data.

5   Examples

The examples below are provided with the code and are used to benchmark observations to model results.

5.1 Utgard High

The Utgard sill complex is part of the North Atlantic Igneous Province (NAIP) in the Vøring and Møre Basins, offshore Norway. This region underwent massive volcanic activity at the Paleocene-Eocene boundary around ~55 Ma (Aarnes et al., 2015). The Utgard High borehole 6607/5-2 was drilled through two sills emplaced in the Upper Cretaceous sedimentary layers. The drilled lithological column consists of nine layers with the oldest being deposited 100 Ma (NPD Factpages, http://factpages.npd.no/factpages/) (Figure 5). For simplicity, the material properties of the entire sedimentary column is set to constant values with the exception of TOC content. TOC content of the Paleocene and Upper Cretaceous sedimentary layers are set to an initial value of 0.6 and 1.5 wt%, respectively. Carbonate and erosional layers are not considered. The modelled sedimentary layers are

379   sequentially deposited at the sedimentation rate calculated from the layer top ages. The two sills are

380   emplaced simultaneously within the Nise and Kvitnos Formations at 55 Ma at a temperature of 1150°C.

381   Sedimentary rocks around the emplaced sills are progressively heated as the sills cool. The vitrinite

382   reflectance values increase and the TOC content reduced by thermally degrading organic matter to form

383   CO_2 (Figure 6). Sedimentation after sill emplacement results in further burial and extension to produce

384   the present-day sedimentary column. Vitrinite reflectance and TOC data from the Norwegian Petroleum

385   Directorate (NPD) and a previous study (Aarnes et al., 2015) are used to benchmark the model and

386   match very well with the modelled results (Figure 7). Further information about the geological and

387   model setting can be found in Aarnes et al. (2015) and the input file '1d_sill_input_utgard.xlsx'.
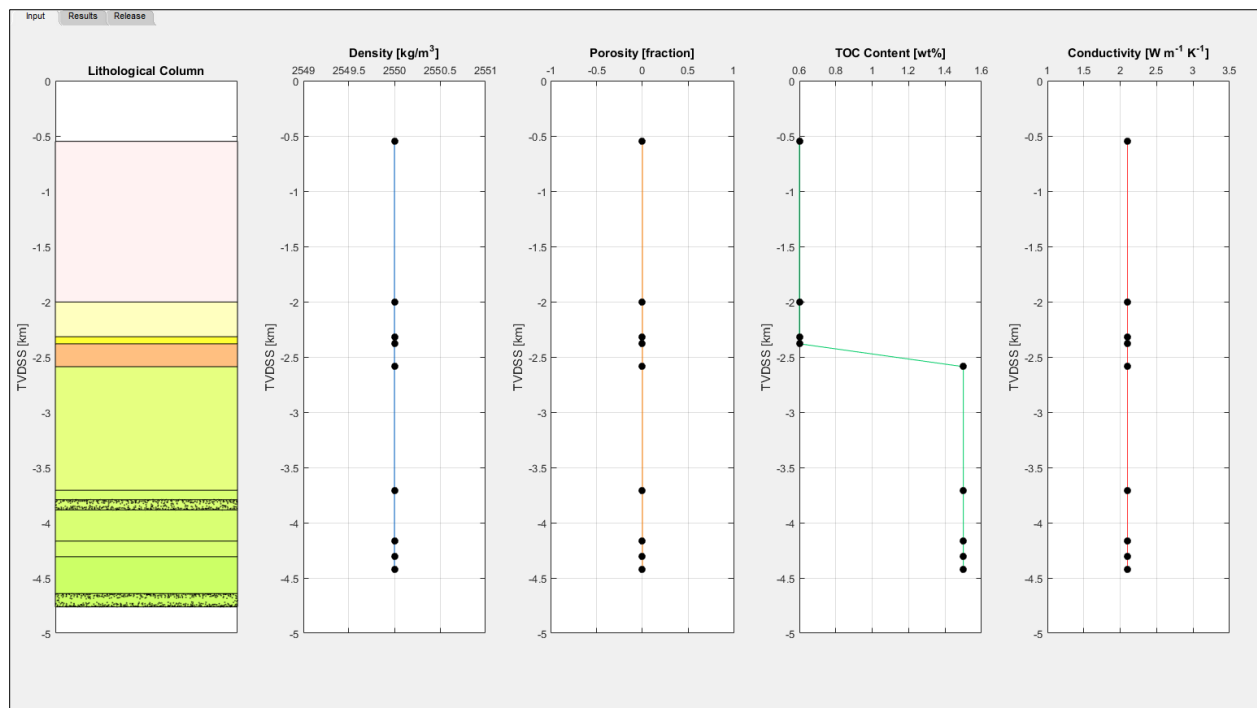
389   *Figure 5. Input tab for the Utgard High example.*
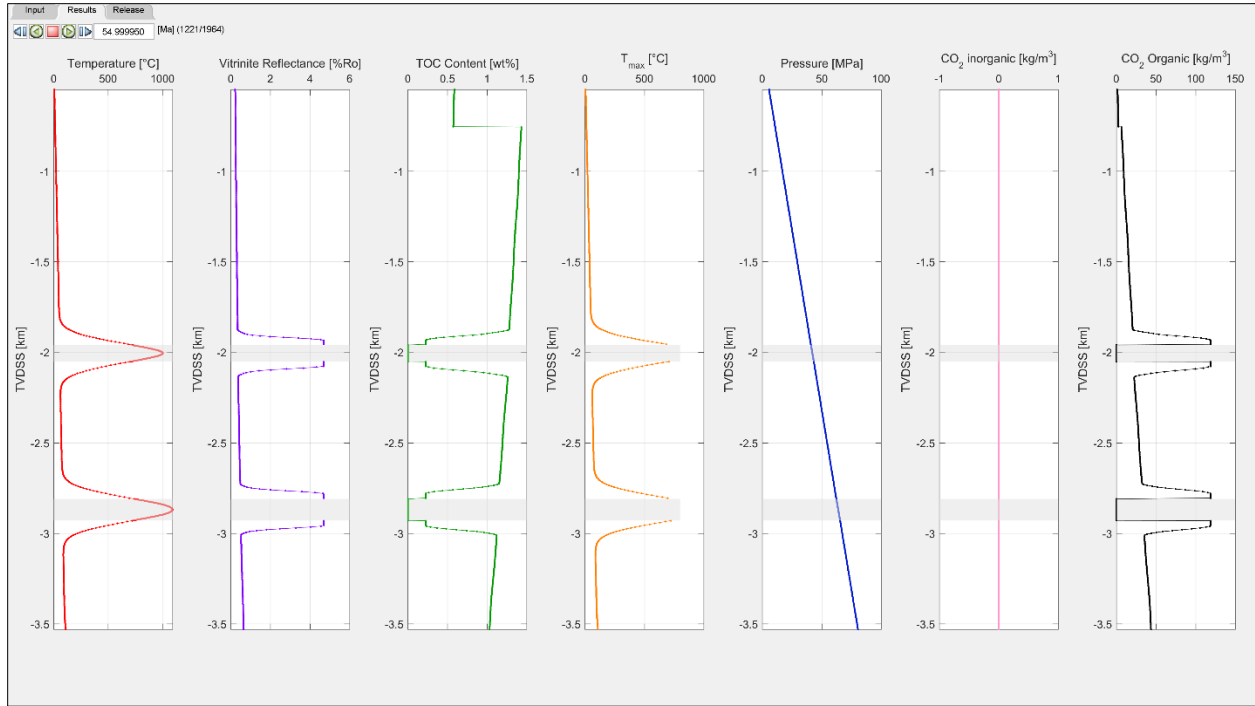
390

391   *Figure 6. Results tab 50 years after the emplacement of sills at 55 Ma for the Utgard High example.*

392   *Sediments around the sills are heated and CO₂ is liberated as organic matter is thermally degraded.*

393

394
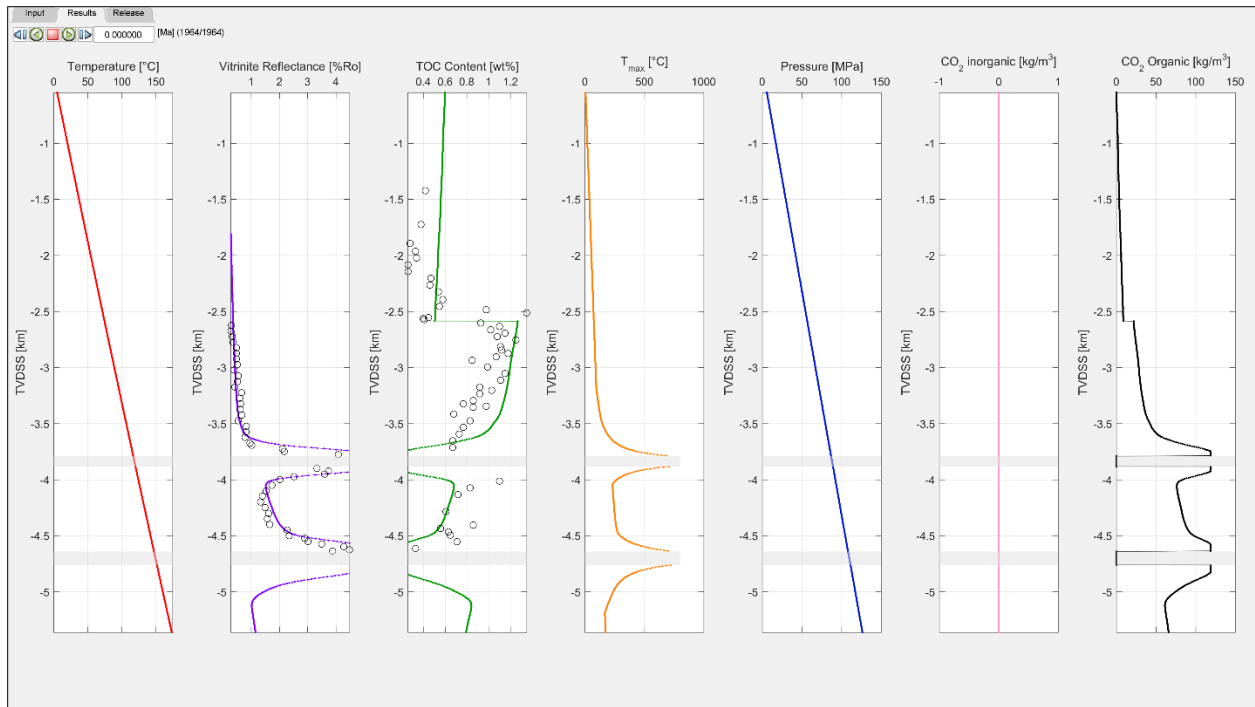
 Figure 7. Results tab at the end of simulation time for the Utgard High example. The present-day VR and

 TOC values (circles) show a good match with the model results.

397

5.2 Karoo

399 The Karoo Large igneous province was emplaced through the Karoo Basin in South Africa in the Early

400 Jurassic. The basin contains sills and dykes of varying thickness (Chevallier and Woodford, 1999; du Toit,

401 1920; Svensen et al., 2015; Walker and Poldervaart, 1949) , emplaced at about 182.6 Ma (Svensen et al.,

402 2012). The basin stratigraphy consists of the Upper Carboniferous to the Triassic Karoo Supergroup and

403 is divided in five groups (the Dwyka, Ecca, Beaufort, Stormberg and Drakensberg groups) with a

404 postulated maximum cumulative thickness of 12 km and a preserved maximum thickness of 5.5 km

405 (Tankard et al., 2009). The depositional environments of the sediments range from marine and glacial

406 (the Dwyka Group), marine to deltaic (the Ecca Group), to fluvial (the Beaufort Group) and finally eolian

407 (the Stormberg Group) (Catuneanu et al., 1998). The Karoo Basin is overlain by 1.65 km of preserved

408 volcanic rocks of the Drakensberg Group, consisting mainly of stacked basalt flows erupted in a

409 continental and dry environment (e.g., (Duncan et al., 1984)). Several recent studies have been devoted

410 to contact metamorphism of the organic-rich Ecca Group (Aarnes et al., 2011b; Moorcroft and

411 Tonnelier, 2016) and the possible consequences of thermogenic methane venting on the Early Jurassic

412 climate (Svensen et al., 2007; Svensen et al., 2015). Here we present two borehole cases from the

413 central (borehole KL1/78) and eastern (borehole LA1/68) parts of the basin previously studied and

414 modelled by Aarnes et al. (2011b) and Svensen et al. (2015), respectively. The details regarding the

415 relative timing of sill emplacement is poorly constrained and we thus use the same age for all sills. If the

416 sills are closely spaced, this will result in a higher maximum temperature in the sedimentary rocks

417 between the sills (cf. (Aarnes et al., 2011b)). For the erosion history of the Karoo Basin, we refer to

418 Braun et al. (2014) and a rapid Late Cretaceous erosion event.

5.2.1 Karoo KL1/78

420 The first example from the Karoo Basin is a short borehole with a length of 136 m that penetrates the

421 Tierberg, Whitehill and Prince Albert Formations. However, these Formations underlie a massive erosion

422 sequence consisting of 2.5 km of extrusives (Drakensberg Group) and 1.5 km of sediments (Stormberg

423 and Beaufort Groups) and are also included in the model. The borehole penetrates a single 15m thick sill

424 at a depth of 72m (Figure 8). The sill is emplaced within the Prince Albert Formation at 182.6 Ma at a

425   temperature of 1150°C. Initial average TOC data for the sedimentary layers away from the sill intrusion

426   is not known but can be roughly estimated using present-day values, i.e. the TOC values will be higher

427   than current values as TOC is thermally broken down close to the intrusion. The initial input TOC data is

428   subsequently refined so that a better match of the model results to the observed data is obtained,

429   thereby highlighting how the model can be used to constrain initial conditions within the sedimentary

430   column (Figure 9). The importance of considering the entire basin history when constructing the model

431   is also emphasized by the VR results. The values of the VR results unaffected by the sill would be much

432   lower than the observed values if the eroded sequences are not considered. Addition of these layers to

433   the model results in added burial than would be expected than by just using the 136 m deep borehole.

434   This translates the VR curve laterally thereby better fitting the observed values (Figure 9). The final

435   model shows a good fit of TOC and VR to present day values. Model input data can be found in

436   '1d_sill_input_kl178.xlsx'.

437
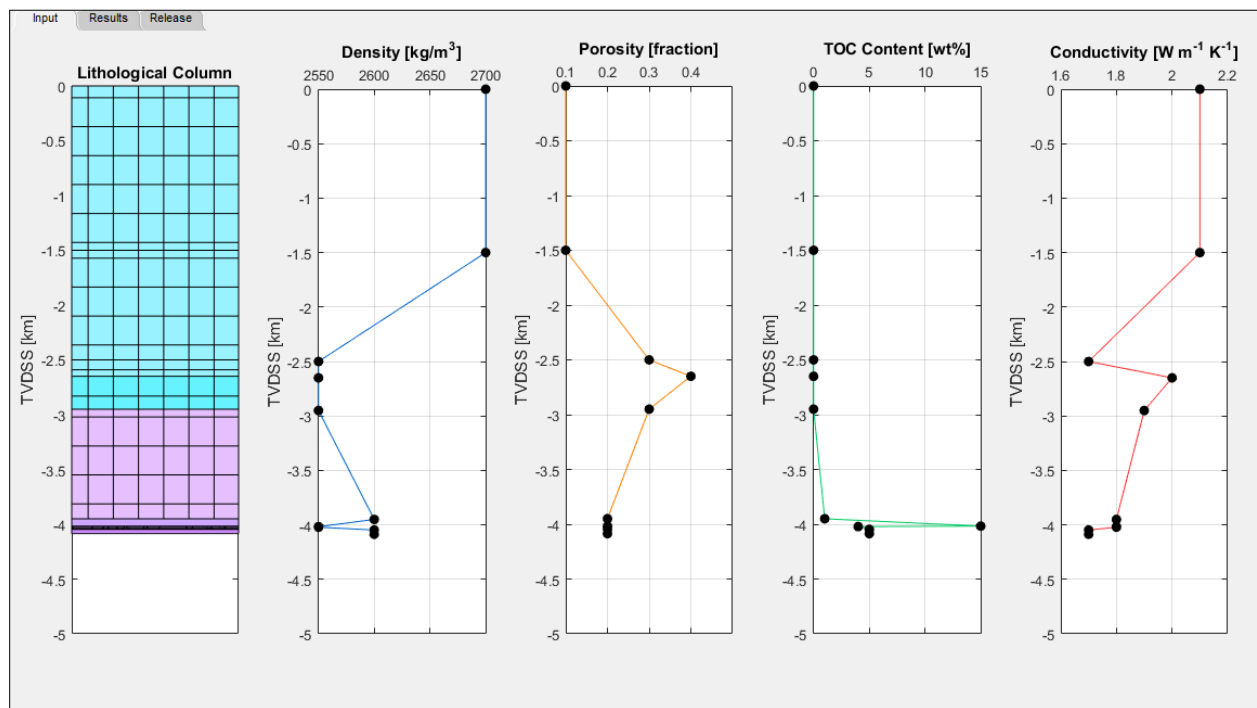
438

439   *Figure 8. Input tab for KL1/78.*
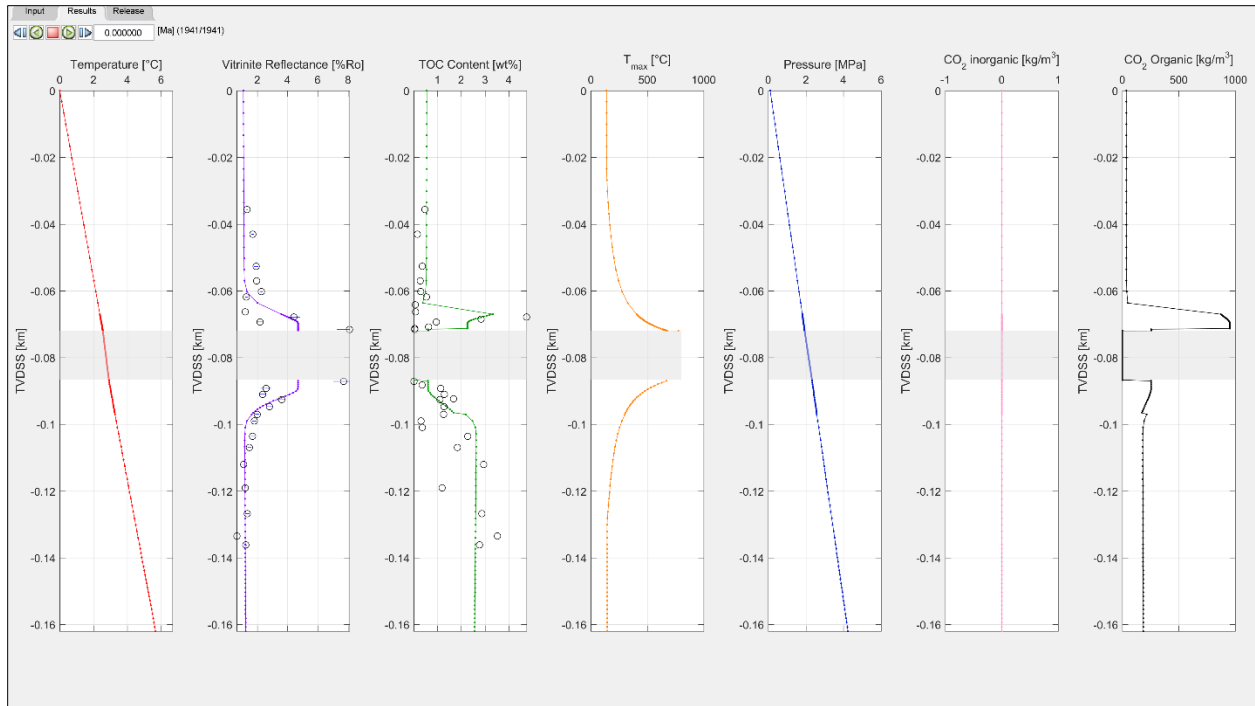
440

441 *Figure 9. Results tab at the end of simulation time for KL1/78 shows a good match to present-day TOC*
442 *and VR values.*

443

5.2.2   Karoo LA1/68

445 The second example from the Karoo Basin is a borehole with a length of 1711 m that penetrates the
446 basin down to the basement (Svensen et al., 2015). Additional erosional sequence consisting mostly of
447 the Drakensberg lavas and a minor section of the Stormberg Group is also added. The borehole
448 penetrates multiple sills throughout the entire column with thicknesses ranging from 2 to 132m (Figure
449 10). Initial average TOC data for the sedimentary layers is estimated from present-day values. Similar to
450 the previous example, material properties are iteratively changed within realistic bounds to arrive at an
451 initial setup that matches the final observations well (Figure 11). Model input data can be found in
452 '1d_sill_input_la168.xlsx'.
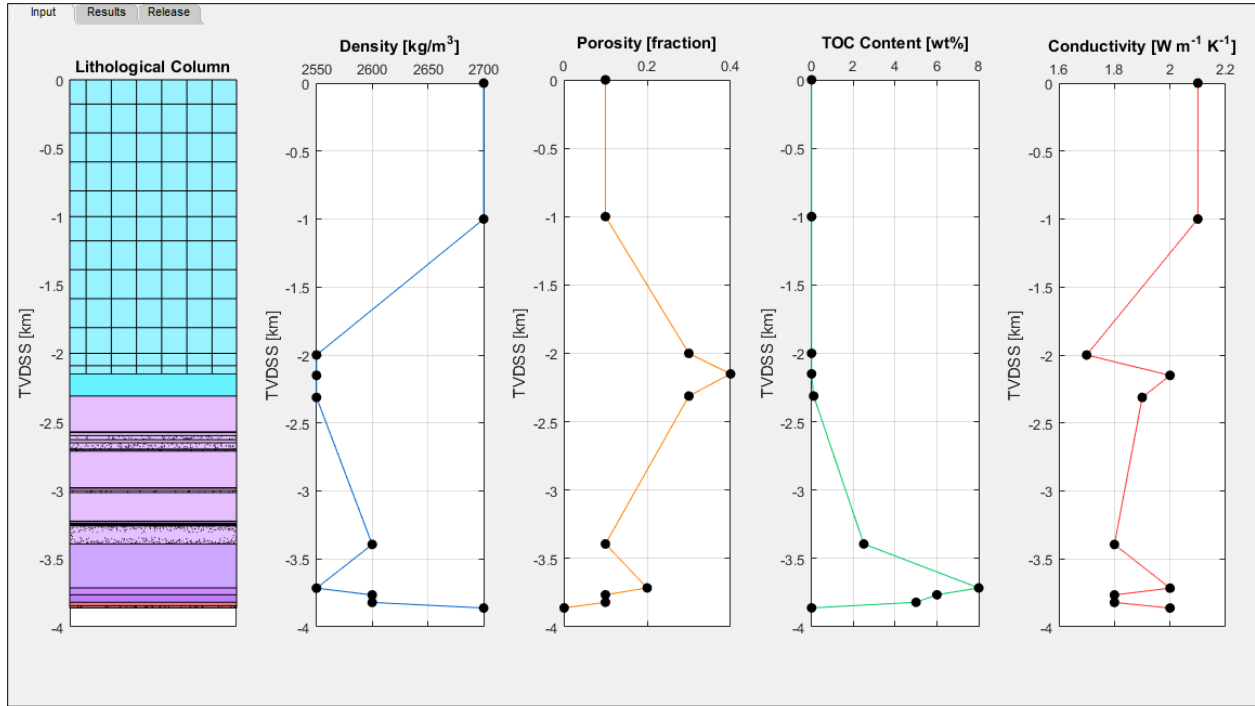
453

454 *Figure 10. Input tab for LA1/68.*
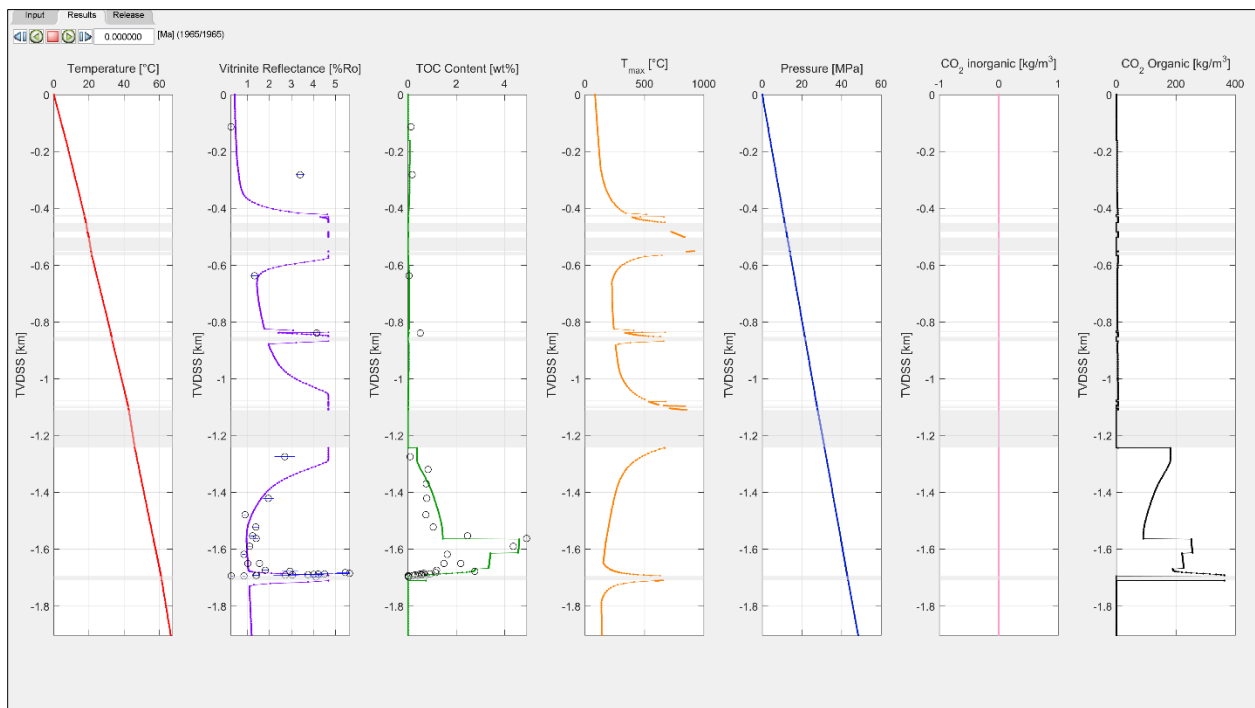
455

456 *Figure 11. Results tab at the end of simulation time for LA1/68 shows a good match to present-day TOC*

457 *and VR values.*

458

5.3   Intrusion into a Pluton

This example has been added to provide an instance where the user may be interested in modelling the thermal aureole of an emplaced sill or dyke but without the effects associated with deposition of sedimentary layers and the thermal evolution of a basin, e.g. emplacement within an igneous or metamorphic rock. Here, we consider an emplacement of a 100m thick sill into a 1.2km thick igneous body that has cooled to a uniform temperature of 30°C (Figure 12). The host rock is constructed by defining a top and bottom layer with the same material properties and ages that are very close to each other (the code does not allow for two layers with the exact same age). In this example the top and bottom layers have ages of 10 and 10.0001 Ma, respectively, and the intrusion is emplaced at 1 Ma. A constant temperature for the host rock is defined by assigning the same temperature, 30°C, to both intervals in the temperature tab of the excel input file. Thus, the thermal evolution of the intrusion can be investigated independent of burial effects of a sedimentary basin if so desired (Figure 13). Further information about the model setting can be found in the input file '1d_sill_input_dyke.xlsx'.
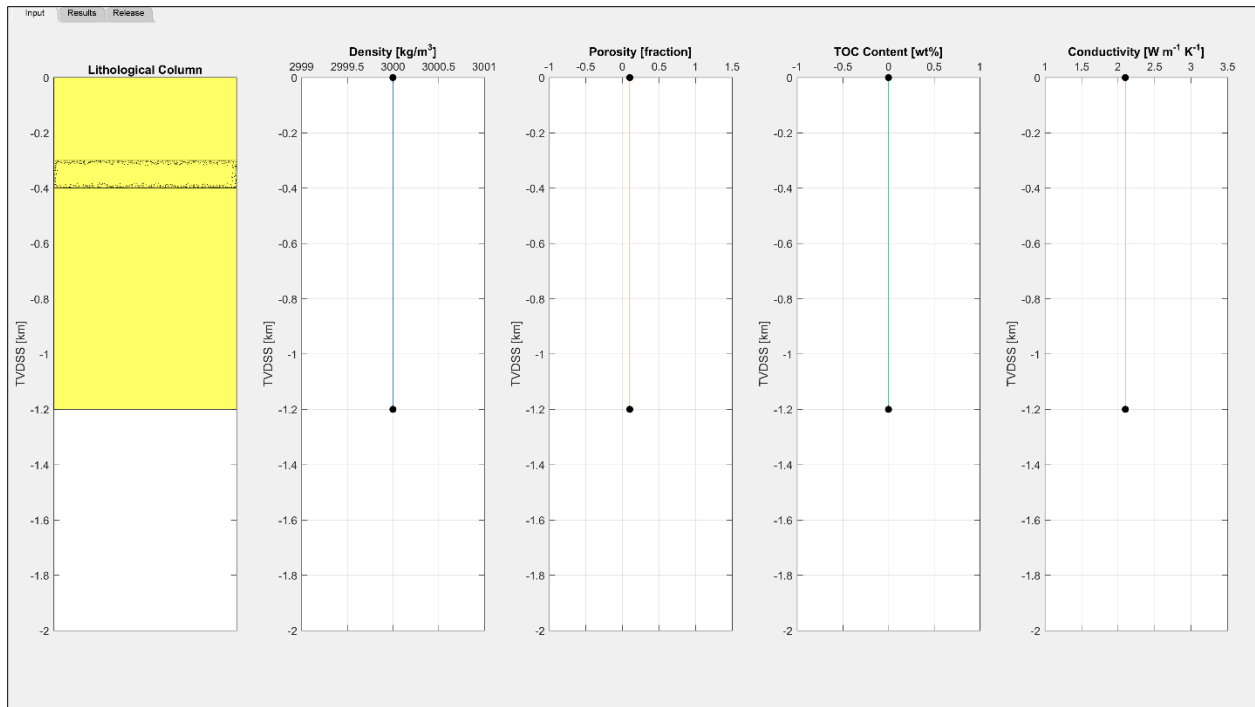
472

473   *Figure 12. Input tab for the Pluton example.*

474
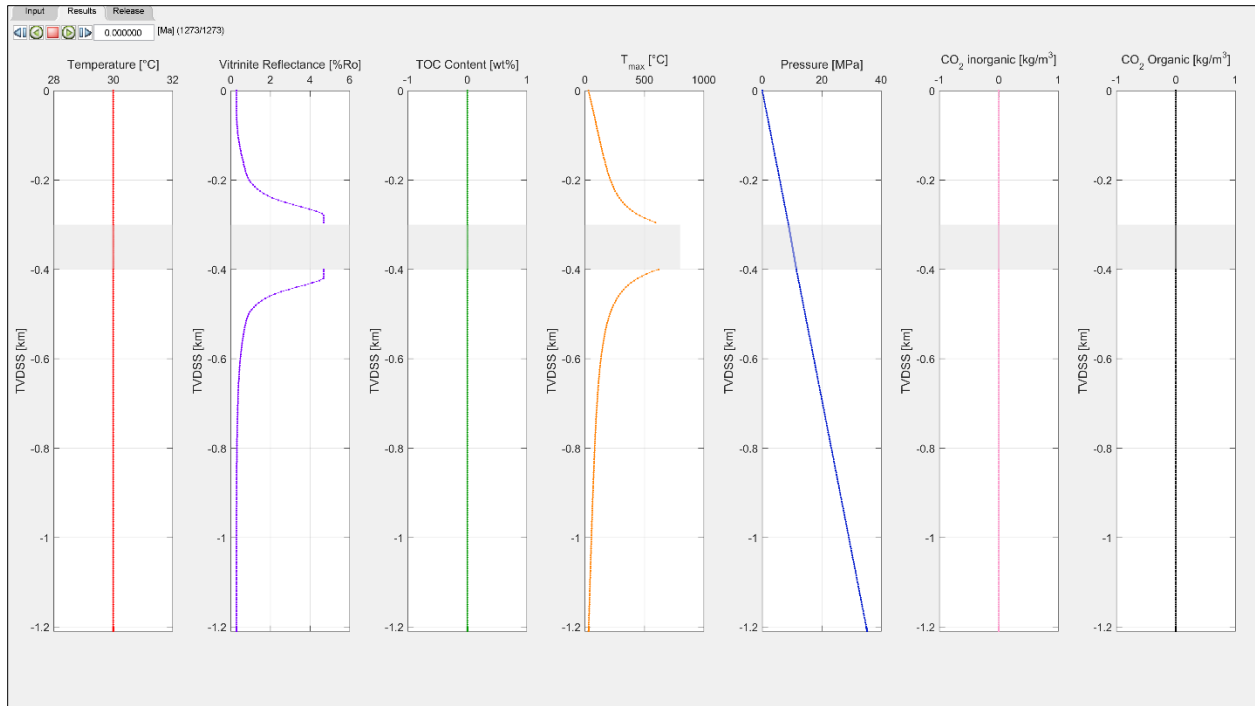
Figure 13. Results tab at the end of simulation time for the pluton example. VR and TOC data are not present for this hypothetical case.

477

6   Conclusions

- SILLi is a numerical model quantifies the thermal evolution of contact aureoles around sills emplaced in sedimentary basins. The model includes basin history (burial and erosion), thus providing background-maturation levels of organic matter and consequently more realistic gas production estimates.

- SILLi is a user-friendly tool that is written in Matlab and uses Excel for input data.

- The 1D tool allows for the quick quantification of the thermal effects of sill intrusions. The results can be, therefore, used to further constrain and test the initial conditions that may have been present within the lithological column that match present-day observations.

- Model output includes peak temperature profiles, post-metamorphic TOC content, vitrinite reflectivity, and the cumulative amount and rate of CO_2 generation. These values can be readily upscaled to basin scales if the sill extent is known. The amount of CO_2 can also be easily converted to other carbon-bearing gases such as CH_4.

491   •   Our three case studies demonstrate a good fit between aureole data (TOC and vitrinite
492   reflectivity) and model output showing that the model can be successfully applied to basins in
493   various global settings.

494

7   Code Availability and Software Requirements

496 The source code with examples is archived on Zenodo (DOI: https://doi.org/10.5281/zenodo.1035878).
497 The Github repository will be regularly updated with improvements and fixes
498 (https://github.com/khiyer/SILLi). Matlab 2014b or higher is required to run the code and Microsoft
499 Excel or any equivalent software is required to edit .xls files.

500

8   License (BSD-2-Clause)

518 The software includes errorbarxy.m by Qi An (2016) (BSD-2-Clause License)
519 (http://www.mathworks.com/matlabcentral/fileexchange/40221).

520

9   Author Contributions

K. Iyer and D.W. Schmid developed the code. K. Iyer implemented the code and wrote the manuscript. H. Svensen guided code development and provided input data from field studies. D. W. Schmid and H. Svensen edited the manuscript.

10   Competing Interests

The authors declare that they have no conflict of interest.

11   Acknowledgements

The authors would like to thank two anonymous reviewers for their constructive reviews which helped us better evaluate the model and manuscript.

12   References

Aarnes, I., Fristad, K., Planke, S., and Svensen, H.: The impact of host-rock composition on devolatilization of sedimentary rocks during contact metamorphism around mafic sheet intrusions, Geochem. Geophys. Geosyst., 12, Q10019, 2011a.

Aarnes, I., Planke, S., Trulsvik, M., and Svensen, H.: Contact metamorphism and thermogenic gas generation in the Vøring and Møre basins, offshore Norway, during the Paleocene–Eocene thermal maximum, Journal of the Geological Society, doi: 10.1144/jgs2014-098, 2015. 588-598, 2015.

Aarnes, I., Svensen, H., Connolly, J. A. D., and Podladchikov, Y. Y.: How contact metamorphism can trigger global climate changes: Modeling gas generation around igneous sills in sedimentary basins, Geochimica Et Cosmochimica Acta, 74, 7179-7195, 2010.

Aarnes, I., Svensen, H., Polteau, S., and Planke, S.: Contact metamorphic devolatilization of shales in the Karoo Basin, South Africa, and the effects of multiple sill intrusions, Chemical Geology, 281, 181-194, 2011b.

Archer, S. G., Bergman, S. C., Iliffe, J., Murphy, C. M., and Thornton, M.: Palaeogene igneous rocks reveal new insights into the geodynamic evolution and petroleum potential of the Rockall Trough, NE Atlantic Margin, Basin Research, 17, 171-201, 2005.

Braun, J., Guillocheau, F., Robin, C., Baby, G., and Jelsma, H.: Rapid erosion of the Southern African Plateau as it climbs over a mantle superswell, Journal of Geophysical Research: Solid Earth, 119, 6093-6112, 2014.

Catuneanu, O., Hancox, P., and Rubidge, B.: Reciprocal flexural behaviour and contrasting stratigraphies: a new basin development model for the Karoo retroarc foreland system, South Africa, Basin Research, 10, 417-439, 1998.

Chevallier, L. and Woodford, A.: Morpho-tectonics and mechanism of emplacement of the dolerite rings and sills of the western Karoo, South Africa, S. Afr. J. Geol., 102, 43-54, 1999.

557 Connolly, J. and Petrini, K.: An automated strategy for calculation of phase diagram sections and
558 retrieval of rock properties as a function of physical conditions, Journal of Metamorphic Geology, 20,
559 697-708, 2002.
560 du Toit, A. L.: the Karroo dolerites of south Africa: a study in hypabyssal injection, S. Afr. J. Geol., 23, 1-
561 42, 1920.
562 Duncan, A., Erlank, A., Marsh, J., and Cox, K.: Regional geochemistry of the Karoo igneous province,
563 1984. 1984.
564 Fjeldskaar, W., Helset, H. M., Johansen, H., Grunnaleiten, I., and Horstad, I.: Thermal modelling of
565 magmatic intrusions in the Gjallar Ridge, Norwegian Sea: implications for vitrinite reflectance and
566 hydrocarbon maturation, Basin Research, 20, 143-159, 2008.
567 Galushkin, Y. I.: Thermal effects of igneous intrusions on maturity of organic matter: A possible
568 mechanism of intrusion, Organic Geochemistry, 26, 645-658, 1997.
569 Hantschel, T. and Kauerauf, A. I.: Fundamentals of Basin and Petroleum Systems Modeling, Springer-
570 Verlag Berlin Heidelberg, 2009.
571 Iyer, K., Rüpke, L., and Galerne, C. Y.: Modeling fluid flow in sedimentary basins with sill intrusions:
572 Implications for hydrothermal venting and climate change, Geochemistry, Geophysics, Geosystems, 14,
573 5244-5262, 2013.
574 Iyer, K., Schmid, D. W., Planke, S., and Millett, J.: Modelling hydrothermal venting in volcanic
575 sedimentary basins: Impact on hydrocarbon maturation and paleoclimate, Earth and Planetary Science
576 Letters, 467, 30-42, 2017.
577 Jaeger, J.: Thermal effects of intrusions, Reviews of Geophysics, 2, 443-466, 1964.
578 Jaeger, J. C.: The temperature in the neighborhood of a cooling intrusive sheet, Am J Sci, 255, 306-318,
579 1957.
580 Jaeger, J. C.: Temperatures outside a cooling intrusive sheet, Am J Sci, 257, 44-54, 1959.
581 Jamtveit, B., Bucher-Nurminen, K., and Stijfhoorn, D. E.: Contact Metamorphism of Layered Shale-
582 Carbonate Sequences in the Oslo Rift: I. Buffering, Infiltration, and the Mechanisms of Mass Transport,
583 Journal of Petrology, 33, 377-422, 1992.
584 Jamtveit, B., Svensen, H., Podladchikov, Y. Y., and Planke, S.: Hydrothermal vent complexes associated
585 with sill intrusions in sedimentary basins. In: Physical Geology of High-Level Magmatic Systems,
586 Breitkreuz, C. and Petford, N. (Eds.), Geological Society Special Publication, Geological Soc Publishing
587 House, Bath, 2004.
588 Kjoberg, S., Schmiedel, T., Planke, S., Svensen, H. H., Millett, J. M., Jerram, D. A., Galland, O., Lecomte, I.,
589 Schofield, N., and Haug, Ø. T.: 3D structure and formation of hydrothermal vent complexes at the
590 Paleocene-Eocene transition, the Møre Basin, mid-Norwegian margin, Interpretation, 5, SK65-SK81,
591 2017.
592 Lovering, T.: Theory of heat conduction applied to geological problems, Geological Society of America
593 Bulletin, 46, 69-94, 1935.
594 Malthe-Sorenssen, A., Planke, S., Svensen, H., and Jamtveit, B.: Formation of saucer-shaped sills. In:
595 Physical Geology of High-Level Magmatic Systems, Breitkreuz, C. and Petford, N. (Eds.), Geological
596 Society Special Publication, Geological Soc Publishing House, Bath, 2004.
597 Monreal, F. R., Villar, H. J., Baudino, R., Delpino, D., and Zencich, S.: Modeling an atypical petroleum
598 system: A case study of hydrocarbon generation, migration and accumulation related to igneous
599 intrusions in the Neuquen Basin, Argentina, Marine and Petroleum Geology, 26, 590-605, 2009.
600 Moorcroft, D. and Tonnelier, N.: Contact Metamorphism of Black Shales in the Thermal Aureole of a
601 Dolerite Sill Within the Karoo Basin. In: Origin and Evolution of the Cape Mountains and Karoo Basin,
602 Springer, 2016.

603 Muirhead, D. K., Bowden, S. A., Parnell, J., and Schofield, N.: Source rock maturation owing to igneous
604 intrusion in rifted margin petroleum systems, Journal of the Geological Society, doi: 10.1144/jgs2017-
605 011, 2017. 2017.
606 Peace, A., McCaffrey, K., Imber, J., Hobbs, R., van Hunen, J., and Gerdes, K.: Quantifying the influence of
607 sill intrusion on the thermal evolution of organic-rich sedimentary rocks in nonvolcanic passive margins:
608 an example from ODP 210-1276, offshore Newfoundland, Canada, Basin Research, 29, 249-265, 2017.
609 Pepper, A. S. and Corvi, P. J.: Simple kinetic models of petroleum formation. Part I: oil and gas
610 generation from kerogen, Marine and Petroleum Geology, 12, 291-319, 1995.
611 Planke, S., Rasmussen, T., Rey, S. S., and Myklebust, R.: Seismic characteristics and distribution of
612 volcanic intrusions and hydrothermal vent complexes in the Vøring and Møre basins. In: Petroleum
613 Geology: North-western Europe and global perspectives - Proceedings of the 6th Petroleum Geology
614 Conference., Doré, A. G. and Vining, B. A. (Eds.), Geological Society, London, 2005.
615 Svensen, H., Corfu, F., Polteau, S., Hammer, O., and Planke, S.: Rapid magma emplacement in the Karoo
616 Large Igneous Province, Earth and Planetary Science Letters, 325, 1-9, 2012.
617 Svensen, H. and Jamtveit, B.: Metamorphic Fluids and Global Environmental Changes, ELEMENTS, 6,
618 179-182, 2010.
619 Svensen, H., Planke, S., Chevallier, L., Malthe-Sørenssen, A., Corfu, F., and Jamtveit, B.: Hydrothermal
620 venting of greenhouse gases triggering Early Jurassic global warming, Earth and Planetary Science
621 Letters, 256, 554-566, 2007.
622 Svensen, H., Planke, S., Malthe-Sorensen, A., Jamtveit, B., Myklebust, R., Rasmussen Eidem, T., and Rey,
623 S. S.: Release of methane from a volcanic basin as a mechanism for initial Eocene global warming,
624 Nature, 429, 542-545, 2004.
625 Svensen, H., Planke, S., Polozov, A. G., Schmidbauer, N., Corfu, F., Podladchikov, Y. Y., and Jamtveit, B.:
626 Siberian gas venting and the end-Permian environmental crisis, Earth and Planetary Science Letters, 277,
627 490-500, 2009.
628 Svensen, H. H., Planke, S., Neumann, E.-R., Aarnes, I., Marsh, J. S., Polteau, S., Harstad, C. H., and
629 Chevallier, L.: Sub-Volcanic Intrusions and the Link to Global Climatic and Environmental Changes, 2015.
630 2015.
631 Sweeney, J. and Burnham, A. K.: Evaluation of a simple model of vitrinite reflectance based on chemical
632 kinetics, AAPG Bulletin, 74, 1559-1570, 1990.
633 Tankard, A., Welsink, H., Aukes, P., Newton, R., and Stettler, E.: Tectonic evolution of the Cape and
634 Karoo basins of South Africa, Marine and Petroleum Geology, 26, 1379-1412, 2009.
635 Tracy, R. J. and Frost, B. R.: Phase equilibria and thermobarometry of calcareous, ultramafic and mafic
636 rocks, and iron formations, Reviews in Mineralogy and Geochemistry, 26, 207-289, 1991.
637 Walker, F. and Poldervaart, A.: Karroo dolerites of the Union of South Africa, Geological Society of
638 America Bulletin, 60, 591-706, 1949.
639 Wang, D.: MagmaHeatNS1D: One-dimensional visualization numerical simulator for computing thermal
640 evolution in a contact metamorphic aureole, Computers & Geosciences, 54, 21-27, 2013.
641 Wang, D. and Manga, M.: Organic matter maturation in the contact aureole of an igneous sill as a tracer
642 of hydrothermal convection, Journal of Geophysical Research: Solid Earth, 120, 4102-4112, 2015.
643 Wang, D. Y.: Comparable study on the effect of errors and uncertainties of heat transfer models on
644 quantitative evaluation of thermal alteration in contact metamorphic aureoles: Thermophysical
645 parameters, intrusion mechanism, pore-water volatilization and mathematical equations, International
646 Journal of Coal Geology, 95, 12-19, 2012.
647 Wang, D. Y., Lu, X. C., Song, Y. C., Shao, R., and Qi, T. A.: Influence of the temperature dependence of
648 thermal parameters of heat conduction models on the reconstruction of thermal history of igneous-
649 intrusion-bearing basins, Computers & Geosciences, 36, 1339-1344, 2010.

650   Wang, D. Y. and Song, Y. C.: Influence of different boiling points of pore water around an igneous sill on
651   the thermal evolution of the contact aureole, International Journal of Coal Geology, 104, 1-8, 2012.
652   Wang, D. Y., Song, Y. C., Liu, Y., Zhao, M. L., Qi, T., and Liu, W. G.: The influence of igneous intrusions on
653   the peak temperatures of host rocks: Finite-time emplacement, evaporation, dehydration, and
654   decarbonation, Computers & Geosciences, 38, 99-106, 2012a.
655   Wang, K., Lu, X. C., Chen, M., Ma, Y. M., Liu, K. Y., Liu, L. Q., Li, X. Z., and Hu, W. X.: Numerical modelling
656   of the hydrocarbon generation of Tertiary source rocks intruded by doleritic sills in the Zhanhua
657   depression, Bohai Bay Basin, China, Basin Research, 24, 234-247, 2012b.